

Supporting Information

Balancing near-field enhancement, absorption, and scattering for effective antenna-reactor plasmonic photocatalysis

*Kun Li¹, Nathaniel J. Hogan^{2,3}, Matthew J. Kale^{1,4}, Naomi J. Halas^{2,3,5,6}, Peter Nordlander^{2,3,6}, Phillip
Christopher^{*,1,7,8}*

1. Department of Chemical and Environmental Engineering, University of California, Riverside, Riverside, CA 92521, USA; 2. Department of Physics and Astronomy, Rice University, Houston, TX 77005, USA; 3. Laboratory for Nanophotonics, Rice University Houston, TX 77005, USA; 4. Division of Chemistry and Chemical Engineering, California Institute of Technology, Pasadena, CA 91125, USA; 5. Department of Chemistry, Rice University, Houston, TX 77005, USA; 6. Department of Electrical and Computer Engineering, Rice University, Houston, TX 77005, USA; 7. Program in Materials Science, University of California, Riverside, Riverside, CA 92521, USA; 8. UCR Center for Catalysis, University of California, Riverside, Riverside, CA 92521, USA

Corresponding Author

Email: christopher@engr.ucr.edu

Contents

1. Materials and methods
 2. Additional characterizations on Ag@SiO₂/Pt
 3. Prerequisites for comparison on photocatalytic performance
 4. Supplementary discussions on FDTD simulations
 5. Supplementary discussions on Monte Carlo simulations
 6. Supplementary discussions on electromagnetic field enhancements
- Supplementary References

Figure S1. TEM images of 12 nm (A), 25 nm (B), 50 nm (C), and 100 nm (D) Ag NPs. The size distributions are 12 ± 2 , 25 ± 3 , 51 ± 5 , and 103 ± 8 nm, respectively. All scale bars are 50 nm.

Figure S2. CO oxidation kinetics. (A) CO oxidation rate of as a function of reaction temperature. (B) Activation energy calculation by Arrhenius' equation. Here k is the rate constant, T is the absolute temperature (in Kelvin), A is the pre-exponential factor, E_a is the activation energy (in Joules), and R is the universal gas constant. Note the thermal gradients are consistent across all samples, although measurements in the Harrick reactor bed cause “incorrect” absolute activation barriers.

Figure S3. Spectrum of the light source used for catalyst illumination in intensity-dependent measurements. Light intensity shed on catalysts was held constantly at 668 mW/cm^2 .

Figure S4. Representative plot for CO production rate at a constant thermal rate, with and without illumination. The photocatalytic rate was calculated as the difference between the steady state rate under illumination and the base thermal rate.

Figure S5. Measured intensity-dependent photocatalytic rate and photoenhancement of catalytic activity for CO oxidation with different catalysts loadings in the reactor. Ag(50 nm)@SiO₂/Pt was used as an example. Photocatalytic measurements are normalized to identical thermal rate.

Figure S6. Position-dependent Pt absorption enhancements at the x - y plane for Ag(25 nm)@SiO₂(4 nm)/Pt structures. The outer colorful ring represents the possible positions for a 5 nm Pt NP (dotted circle).

Figure S7. Electromagnetic distribution at the x - y plane for (A) structure with 12 Pt NPs located around Ag(25 nm)@SiO₂(4 nm) and (B) two Pt NPs with a 5 nm distance.

Figure S8. Absorption cross section in Pt (left axis) at four different positions and absorption and scattering cross section in Ag (right axis) for Ag(25 nm)@SiO₂(4 nm)/Pt.

Figure S9. Absorption cross section in Pt (left axis) at four different positions and absorption and scattering cross section in Ag (right axis) for each Ag@SiO₂/Pt heterostructure that contains 25 nm Ag core and SiO₂ shell with varying thicknesses, i.e., (A) 0 nm, (B) 4 nm, (C) 10 nm, and (D) 20 nm.

Figure S10. Absorption cross section in Pt (left axis) and Ag (right axis) (A), ENH_{Abs} (B), Q_{Abs} (C), and U_{Light} (D) as a function of wavelength for Ag@SiO₂/Pt heterostructures comprised of 25 nm Ag core and SiO₂ shell with various thicknesses.

Figure S11. Electromagnetic field distributions in the x - y plane at the wavelengths corresponding to Pt absorption maxima (409 nm for Ag(25 nm)/Pt, 417 nm for Ag(25 nm)@SiO₂(4 nm)/Pt, 425 nm for

Ag(25 nm)@SiO₂(10 nm)/Pt, and 430 nm for Ag(25 nm)@SiO₂(20 nm)/Pt).

Figure S12. Absorption cross section in Pt (left axis) at four different positions and absorption and scattering cross section in Ag (right axis) for each Ag@SiO₂/Pt heterostructure that contains 10 nm SiO₂ shell and Ag core with varying diameters, i.e., (A) 12 nm, (B) 25 nm, (C) 50 nm, and (D) 100 nm.

Figure S13. Absorption cross section in Pt at four different positions (red, green, blue, and purple curves) and Pt position-averaged absorption cross section (dotted black curve) for SiO₂(50 nm)/Pt structure. Absorption cross section in an isolated Pt NP is also shown (solid black curve).

Figure S14. (A) Absorption quality factor (Q_{Abs}), and (B) light utilization coefficient (U_{Light}) for Ag@SiO₂/Pt heterostructures with different Ag NP sizes and a constant 10 nm SiO₂ shell.

Figure S15. (A) Schematic of broadband photocatalysis on 2-D films of Ag@SiO₂/Pt heterostructures. (B, C) Description of the design rules for wavelength selectivity in photocatalysis. (B) Pt absorption cross section for Ag@SiO₂/Pt heterostructures with 10 nm SiO₂ shell and varying diameters of Ag core. The shaded region shows the limits of integration (2.70–2.82 eV. i.e., wavelength range 460–440 nm) when comparing the wavelength selectivity of each structure. (C) The percentage of broadband Pt ENH_{Abs} occurring in the wavelength-selective range of 450±10 nm.

Figure S16. (A) Cartoon of broadband photocatalysis of Ag@SiO₂/Pt heterostructures in 3D reactor geometry. (B) Wavelength-dependent penetration depth for the four proposed heterostructures. The depth is the value where the light intensity decays to 1/e of the maximum (incident light).

Figure S17. Electromagnetic field distributions in the x - y plane at the wavelengths corresponding to Pt absorption maxima (418 nm for Ag(12 nm)@SiO₂(10 nm)/Pt, 425 nm for Ag(25 nm)@SiO₂(10 nm)/Pt, 436 nm for Ag(50 nm)@SiO₂(10 nm)/Pt, and 416 nm for Ag(100 nm)@SiO₂(10 nm)/Pt).

Figure S18. Wavelength-dependent electromagnetic field enhancement values at the Pt surface for the four Ag@SiO₂/Pt heterostructures with different Ag NP sizes.

1. Materials and methods

1.1 Catalysts preparations and characterizations

Synthesis of Ag nanoparticles. Briefly, Ag NPs were synthesized using a seed-growth method described in a previous work^[1] with minor modifications. Ag seeds of ~12 nm in diameter were prepared by injecting 1 mL of AgNO₃ (25 mM) into a boiling aqueous solution (100 mL) containing sodium citrate (5 mM) and tannic acid (0.25 mM) under vigorous stirring. Then, seed solution was diluted and cooled down to 90 °C, followed by a sequentially injection of sodium citrate, tannic acid, and AgNO₃. This process was repeated several times for larger Ag NPs (25, 50, and 100 nm). The Ag NPs were washed with deionized water for 3 times.

Synthesis of Ag@SiO₂ core@shell nanoparticles. The Ag@SiO₂ core@shell NPs with varying SiO₂ shell thickness were formed by employing Ag NPs as cores for tetraethoxysilane (TEOS) hydrolysis developed by Stöber et al.^[2] For example, in the synthesis of Ag@SiO₂(10 nm), ~20 mg of Ag NPs obtained above was dissolved in a mixture of 20 mL of water and 80 mL of ethanol and stirred for 30 min at 600 rpm at 30 °C. Then, 2 mL of ammonia aqueous solution (28 wt%) were added under stirring. 200, 80, 30, or 10 μL (for 12, 25, 50, or 100 nm Ag NPs, respectively) of TEOS was dissolved in 10 mL of ethanol in advance, and introduced into the mixture by a syringe pump within 2 hours. The reaction was continued for 20 hours, and the results were washed with deionized water for 4 times and then dried in vacuum.

Synthesis of SiO₂ nanoparticles. SiO₂ NPs with a diameter of 50 nm were synthesized via a modified Stöber method.^[2] Typically, 50 mL of ethanol solution containing 0.72 mL of H₂O and 2.53 mL of NH₃·H₂O was stirred at 600 rpm at 35 °C for 30 min. Then 1.675 mL of TEOS was quickly added and the mixture was kept stirred for 20 hours. The resultant SiO₂ nanospheres was washed with deionized water for 3 times and then dried in vacuum.

Synthesis of Pt nanoparticles. 40 mL of H₂PtCl₆ (1 mM) and 1.25 mL of sodium citrate (40 mM) aqueous solution were added in a 100 mL three-neck flask at room temperature, and stirred at 600 rpm for 3 min. Then, 2.75 mL of NaBH₄ (0.1 M) solution was added dropwise. After 2 hours, Pt NPs were centrifuged and washed with deionized water.

Assembly of Ag@SiO₂/Pt core@shell/satellites heterostructures. Ag@SiO₂/Pt heterostructures were assembled by an impregnation method. Typically, Ag@SiO₂ (99 mg) was added to Pt NPs (1.0 mg) colloid solution, and sonicated for one hour to facilitate dispersion. Then the mixture was dried in vacuum at 60 °C overnight allowing for all the Pt NPs to adsorb to the Ag@SiO₂ surface. SiO₂/Pt heterostructures, which were used in control experiments, were prepared via a similar method, where SiO₂ nanospheres were used instead of Ag@SiO₂.

Characterizations. Transmission electron microscope (TEM) images were taken with a FEI-Tecnai 12 TEM facility operating at an accelerating voltage of 120 kV. Ultraviolet-visible (UV-Vis) extinction measurements were performed on a Thermo Scientific Evolution 300 spectrophotometer.

1.2 Photocatalytic reactivity measurements

Dilution. The Ag@SiO₂/Pt heterostructures was mixed with commercial SiO₂ gels (60~200 mesh, 150Å, Sigma-Aldrich) by a weight ratio of 1:4 in order to be diluted to 1/5. The mixed powders were dispersed in water (30~40 mL), sonicated, and stirred overnight for better dispersion. The suspension was further evaporated in a rotary evaporation and the dried, fine powders are collected.

Pretreatment. He (99.999%), O₂ (99.999%), H₂ (99.999%), and CO (10% in He) were purchased from Airgas and used as received. All experiments were performed in a Harrick High Temperature Reaction Chamber (which was equipped with a quartz window for catalyst bed illumination) and operated under differential reactor conditions.^[3,4] Firstly, 20.0 mg catalyst was loaded on top of 30.0 mg SiO₂ gels (60-200 mesh, pore size 150 Å, Sigma Aldrich) which were inert and used to raise the bed height and to give an approximate catalyst bed depth of ~2 mm. Prior to use, all catalysts were pretreated *in situ* at atmospheric pressure by flowing 78 sccm (standard cubic centimeters per minute) He and 22 sccm O₂ at 230°C for 1 hour. The catalyst bed was flushed with 100 sccm He for 10 minutes before *in situ* reduction at 230°C for 1 hour using 100 sccm H₂. After flushing the bed once more for 10 minutes with 100 sccm He, the catalysts were exposed to catalytic reaction conditions (see below) and left overnight (typically, ~12 hours) to reach steady state.

Photocatalytic CO oxidation was executed in an atmosphere consisting of 1% CO, 10% O₂ and balance He. All reactions were run with a total flow rate of 100 sccm and the composition of effluent

gases was monitored on-line with a Hiden quadrupole mass spectrometer (MS, model HALO 201) equipped with a secondary electron multiplier detector. CO oxidation was tuned to a constant thermal CO₂ production rate of $\sim 6 \times 10^{+16}$ molecules/s by controlling reaction temperature (227-242°C). This corresponds to $\sim 7\%$ conversion for CO oxidation, which place the reaction in the differential regime.

Catalysts were illuminated by a 1,000 W continuous wave Xenon light source (Newport Corporation model 66870) coupled to a water-cooled IR filter (model 6123NS) and monochromator (model 74100) with optical filters for light intensity control. A liquid light guide attached to the output of the monochromator was used to illuminate the catalyst bed. Light source wavelength and intensity were calibrated before each measurement using a CCD (Avantes AvaSpec-EDU) and thermopile (Newport 818P-010-12). Intensity of a specific wavelength of light did not exceed 120 mW/cm² in the wavelength and intensity dependence experiments. Wavelength- and intensity-dependent reaction rate measurements were performed at steady state, constant temperature and reactant composition.

All intensity-dependent measurements of the photocatalytic rate/photoenhancement and wavelength-dependent measurements of the QY were calculated as the average of three unique measurements and were normalized to the same thermal rate ($6 \times 10^{+16}$ molecules/s) to reduce inconsistencies in QY due to small fluctuations in the thermal rates. The normalization was calculated assuming the QY is linearly proportional to the thermal rate, or exponential with reaction temperature.^[4,5]

1.3 FDTD simulations

The optical properties of Ag@SiO₂/Pt heterostructures were simulated by using the finite-difference-time-domain (FDTD) method for solving Maxwell's equations. In this study, the package (FDTD Solutions; Version 8.15) from Lumerical, Inc, was employed. The modeled structures are illustrated in Figure 3A. The Ag core was modeled as a sphere with different diameters ranging from 12 nm to 100 nm, of which the refractive index was taken from the material database of CRC^[6,7] (provided by FDTD Solutions, Lumerical). The surface of the Ag core was coated with an SiO₂ spacer layer with different shell thicknesses (0 nm, 4 nm, 10 nm, and 20 nm). Finally, Pt NP with a diameter of 5 nm was decorated on the surface of the Ag@SiO₂ structure. The refractive index of SiO₂ and Pt were taken from the material database of Palik^[8] (provided by FDTD Solutions, Lumerical). Various patterns with

different Pt positions were tested. In all cases, Pt NPs were placed on the surface of Ag@SiO₂ in the propagation/polarization plane (the x - y plane) of the incident light field.

Total-field/scattered-field light source conditions were used in all simulations. The incident light injected toward $+y$ direction, and polarized along x -axis. The wavelength was set to be from 350 nm to 700 nm. A non-uniform mesh was used in simulating regions. Graded meshing technology is also employed in order to gradually vary the spatial step in the vicinity of the small Pt NPs. In all cases, we used a mesh step of $d_x=d_y=d_z=0.25$ nm for each Pt NP, a mesh step of $d_x=d_y=d_z=0.5$ nm for smaller Ag@SiO₂ particles (Ag diameter <70 nm), and a mesh step of $d_x=d_y=d_z=1$ nm for larger Ag@SiO₂ particles (Ag diameter >70 nm).

The absorption and scattering were calculated within the total-field/scattered-field formalism. In addition, the standard Fourier transform was carried out to visualize the electromagnetic field distributions in the x - y plane at the each wavelengths.

1.4 Monte Carlo simulations

Monte Carlo approach was used to predict light transport in catalyst beds consisting of Ag@SiO₂/Pt heterostructures dispersed in SiO₂ diluents. The Monte Carlo simulations were custom written in *C*. The experimental geometry of the system was modeled as closely as possible including photocatalytic reactor size and the SiO₂/photocatalyst volumetric dilution ratio. FDTD calculated optical properties of the Ag@SiO₂/Pt heterostructures and the measured broadband spectrum of the light source in photocatalytic experiments were used to simulate each system.

2. Additional characterizations on Ag@SiO₂/Pt

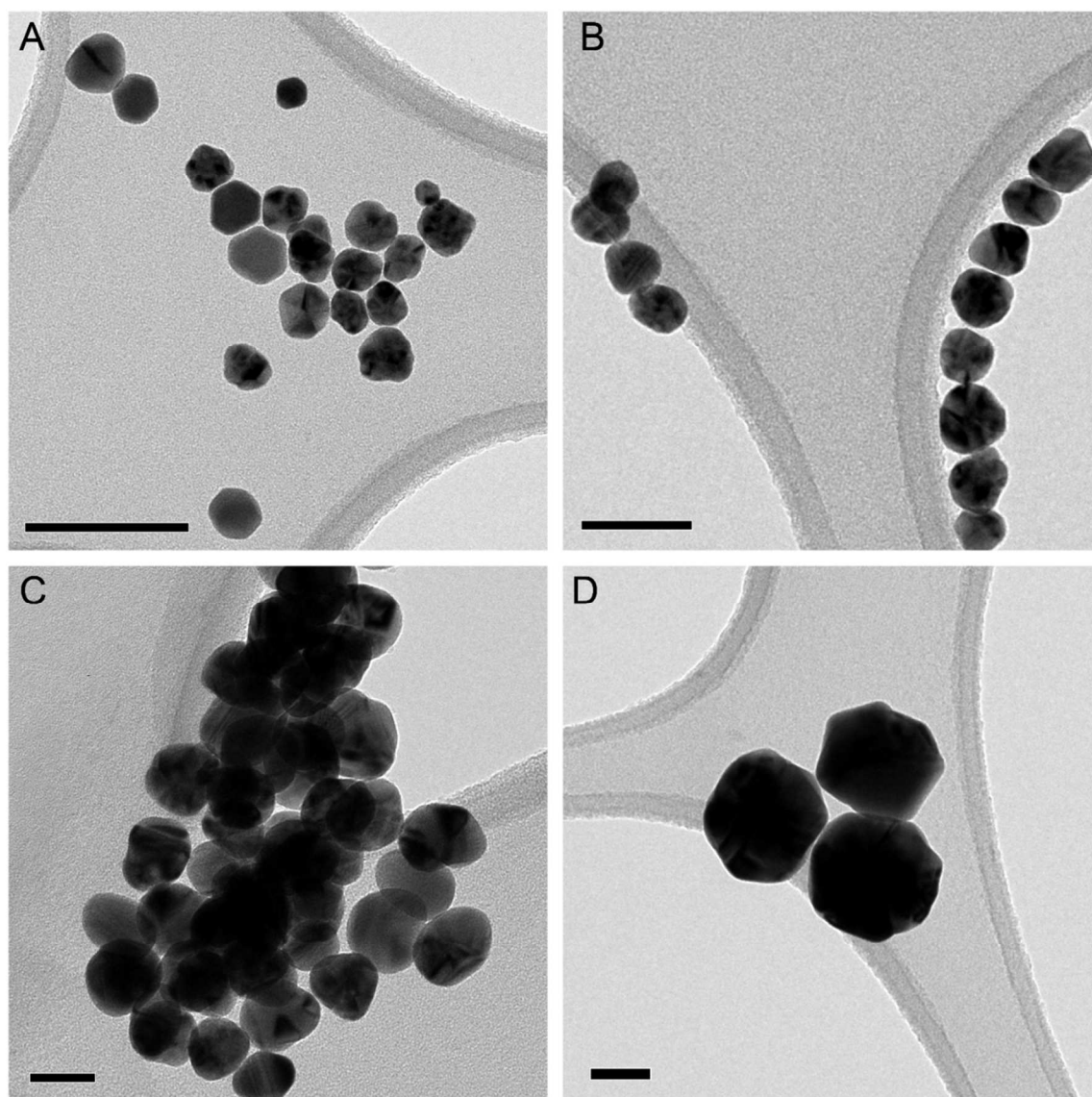


Figure S1. TEM images of 12 nm (A), 25 nm (B), 50 nm (C), and 100 nm (D) Ag NPs. The size distributions are 12 ± 2 , 25 ± 3 , 51 ± 5 , and 103 ± 8 nm, respectively. All scale bars are 50 nm.

Table S1. Plasmon peak wavelength for Ag and Ag@SiO₂ structures in UV-vis extinction measurements

Ag NP's diameter (nm)	Plasmon peak wavelength of Ag	Plasmon peak wavelength of Ag@SiO ₂
12	401 nm	405 nm
25	420 nm	427 nm
50	436 nm	444 nm
100	473 nm	493 nm

3. Prerequisites for comparison on photocatalytic performance

3.1 Thermal reactivity consistency

Ensuring identical thermal catalytic properties of all samples is requisite for making rigorous measurements of the influence of Ag LSPR on photocatalysis by Pt. Kinetic studies (Figure S2) show that photocatalytic rate of CO oxidation and apparent activation energy (E_a) on each Ag@SiO₂/Pt structures are in good agreement with the result for Pt NPs deposited on inert SiO₂. It is noted that the E_a measurements performed in the Harrick reactor is technically “incorrect” if comparing with the results of that in thermal reactor. Although, the consistence of the thermal gradients across all samples proves that we are still consistently in the regime where the Pt surface is poisoned by CO molecule.

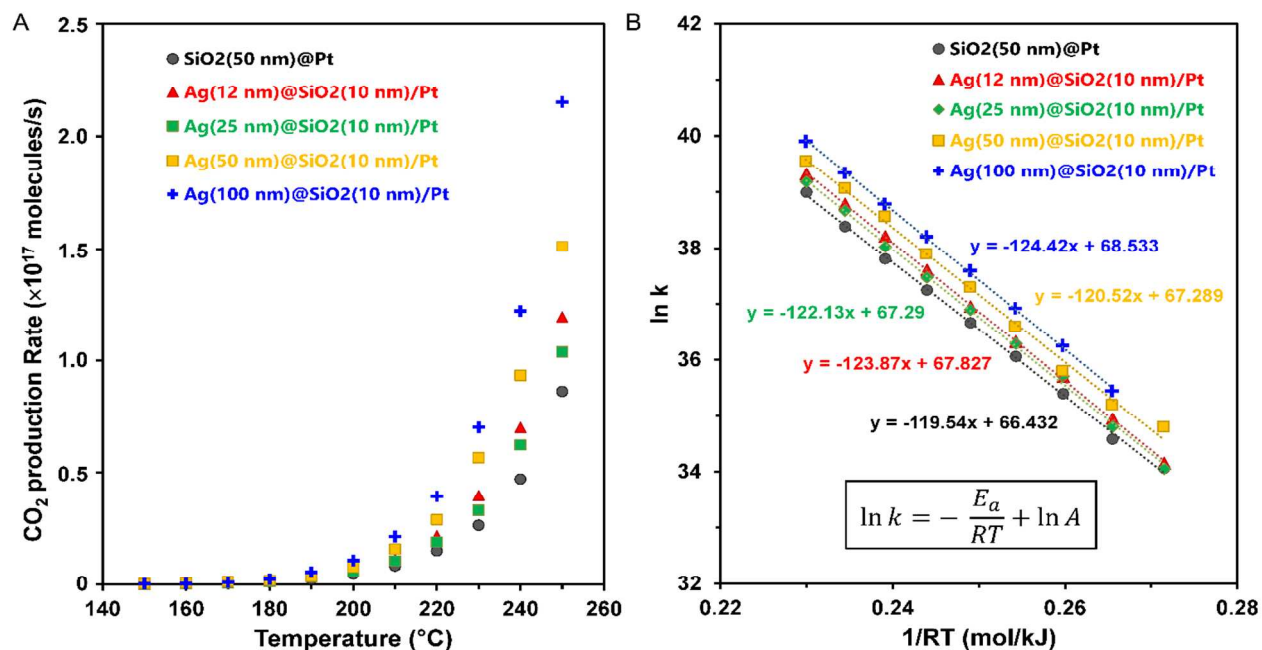


Figure S2. CO oxidation kinetics. (A) CO oxidation rate of as a function of reaction temperature. (B) Activation energy calculation by Arrhenius' equation. Here k is the rate constant, T is the absolute temperature (in Kelvin), A is the pre-exponential factor, E_a is the activation energy (in Joules $\cdot\text{mol}^{-1}$), and R is the universal gas constant. Note the thermal gradients are consistent across all samples, although measurements in the Harrick reactor bed cause “incorrect” absolute activation barriers.

3.2 Low light flux

Photocatalytic measurements were conducted with a low-intensity visible photon flux, where photon-induced reactions on metal surfaces typically occur *via* transient electron localization in normally unoccupied antibonding orbitals associated with adsorbate or adsorbate–metal bonds. Figure S3 shows the spectral output of the light source used in photocatalytic measurements, which was also used in Monte Carlo simulations for light transport analysis (Section 5, Supporting Information).

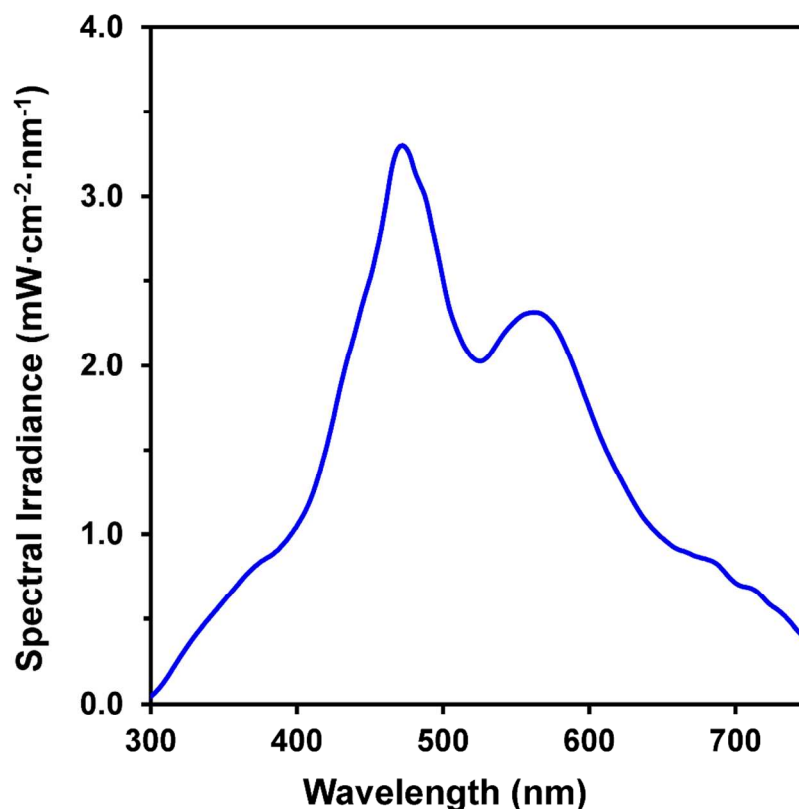


Figure S3. Spectrum of the light source used for catalyst illumination in intensity-dependent measurements. Light intensity shed on catalysts was held constantly at 668 mW/cm².

3.3 Fully reversible photoactivity

The system responded immediately to the introduction and removal of light with no change in the thermal rate, indicating that no structural or chemical changes to the catalysts were induced by illumination (Figure S4). In all photocatalytic measurements, similar background thermal rates were used to ensure there was no influence of the magnitude of the thermal rate on comparison of photocatalytic properties.

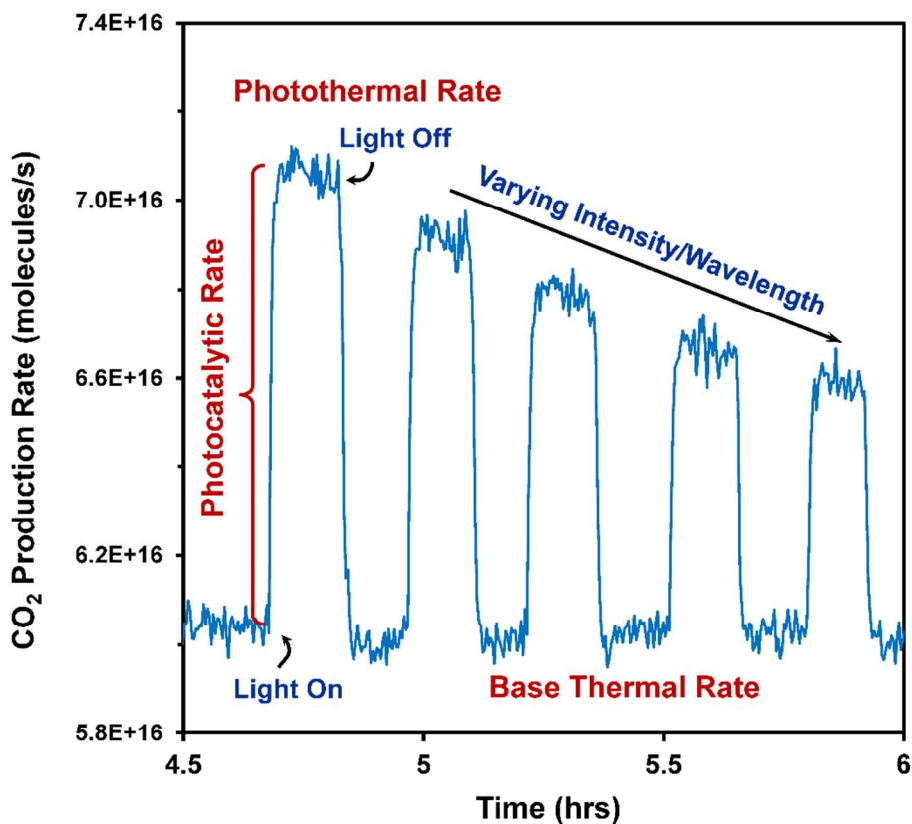


Figure S4. Representative plot for CO production rate at a constant thermal rate, with and without illumination. The photocatalytic rate was calculated as the difference between the steady state rate under illumination and the base thermal rate.

3.4 Working in the light limited regime

The consistency of photocatalytic performance for measurements with 3.22 mg and 4.68 mg of Ag(50 nm)@SiO₂/Pt antenna-reactor complexes (Figure S5) is evidence that sufficient catalysts were added to ensure that no photons propagated on the way through the catalyst bed. In all cases, the system was operated in the light-limited regime, where all photons were extinguished (absorbed/scattered) by catalysts such that increasing the amount of catalysts kept the photocatalytic rate constant.

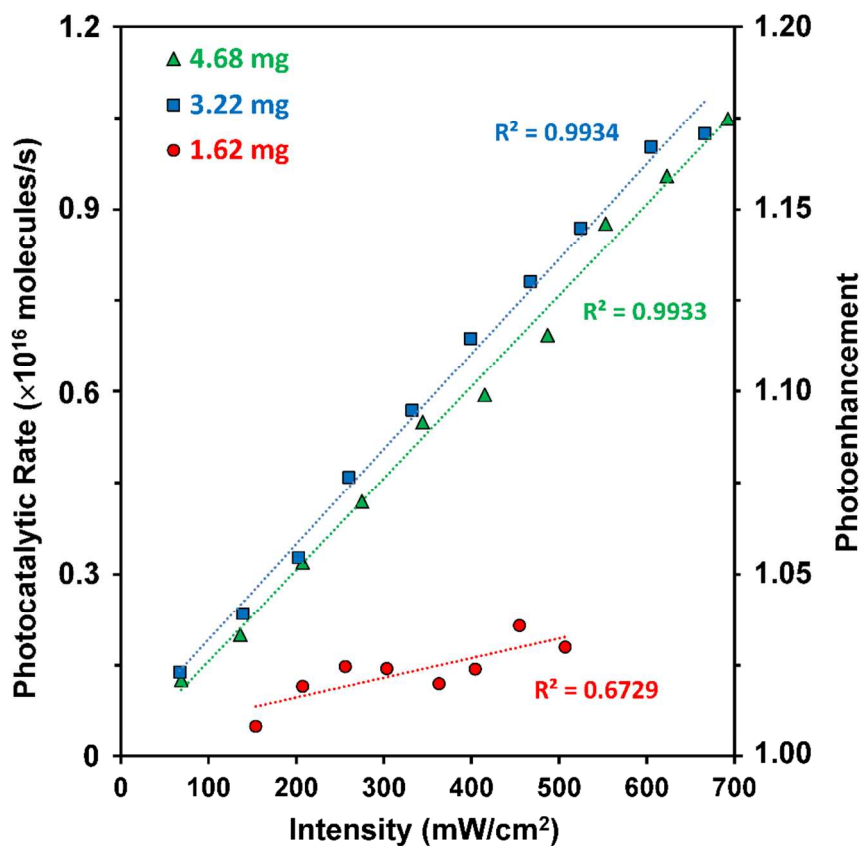


Figure S5. Measured intensity-dependent photocatalytic rate and photoenhancement of catalytic activity for CO oxidation with different catalysts loadings in the reactor. Ag(50 nm)@SiO₂/Pt was used as an example. Photocatalytic measurements are normalized to identical thermal rate.

4. Supplementary discussions on FDTD simulations

4.1 Model settings for FDTD

In our finite-difference time-domain (FDTD) simulations, total-field/scattered-field source conditions were used, where the incident light traveled along the $+y$ direction, and polarized along the x -axis. However, the incident photon flux in our photocatalytic measurements was not polarized and was randomly oriented with respect to the heterostructures. Thus, it is critical to understand the dependence of absorption enhancements in Pt on position at the surface of Ag@SiO₂ and develop an accurate theoretical representation of the average interaction between Pt and Ag under a non-polarized light flux with randomly oriented Pt NPs on the heterostructure, given randomly distributed particles in a non-polarized field that would characterize typical photocatalytic measurements.

4.1.1 Dependence of Pt absorption enhancements on Pt positions

To figure out the dependence of Pt absorption enhancements on Pt positions, we considered one Pt NP decorating the perimeter of an Ag(25 nm)@SiO₂(4 nm) structure at 12 representative positions in the x - y plane (Figure S6).

The outer ring in Figure S6 depicts the absorption enhancement values of Pt NP at different position in the x - y plane, which is the light absorption maximum in Pt for Ag@SiO₂/Pt structures divided by the light absorption in an isolated Pt NP at the same wavelength. The position-dependent Pt absorption enhancements in the x - y plane is bilaterally symmetric, which is easy to understand if taking into account the symmetry of Ag@SiO₂ structure and the nature of the incident light. Therefore, only structures that possess a Pt NP located in the top-right quarter of the model need to be studied.

An accurate representation of the average interaction between Pt and Ag under a non-polarized light flux can be approximated by placing Pt NPs in the top-right quarter at the x - y plane of the Ag@SiO₂ structure at 4 locations from 0 to 90° (Figure 3A) and averaging the response for this range of orientations. Due to the system symmetry, this reasonably represents the behavior of a random distribution of Pt particles under non-polarized illumination.

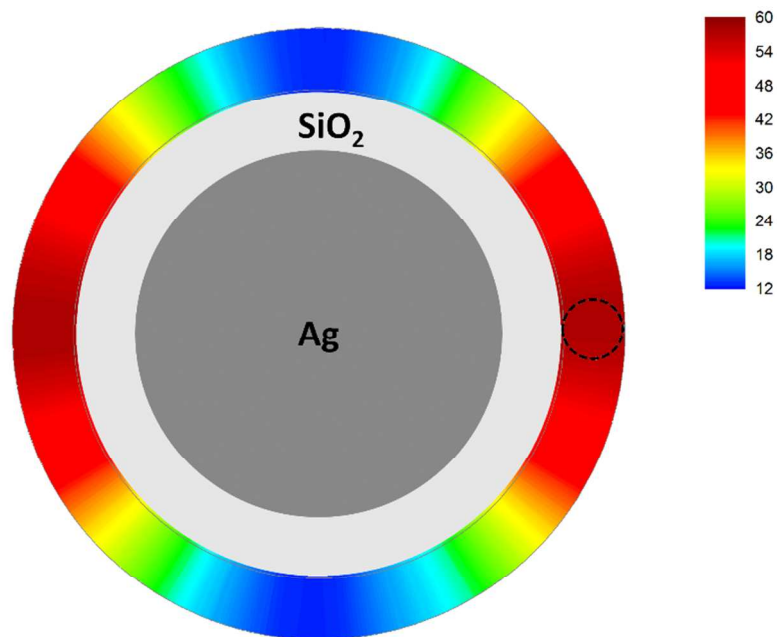


Figure S6. Position-dependent Pt absorption enhancements at the x - y plane for Ag(25 nm)@SiO₂(4 nm)/Pt structures. The outer colorful ring represents the possible positions for a 5 nm Pt NP (dotted circle).

4.1.2 Assumptions for FDTD calculations

It is acceptable that placing Pt particles at positions in the propagation/polarization plane (the x - y plane) can represent any positions where Pt NP could be located around an Ag@SiO₂ sphere. In addition, to simplify the simulation process, we proposed three reasonable assumptions:

(i) In typical photocatalytic reaction systems, Pt weight loadings (usually < 5 wt%) are low enough to ensure that individual Pt NPs are well separated with minimal coupling.

To prove this situation, we carried out FDTD calculation for the structure with 12 Pt NPs located around Ag(25 nm)@SiO₂(4 nm) at the x - y plane, as well as two Pt NPs with a 5 nm distance (Figure S7). No coupling between Pt NPs can be found, indicating a \sim 5 nm distance between individual Pt NPs makes them well separated. In all of our studied structures in this work, the Pt weight loadings (1.0%) guarantee an enough long distance between individual Pt NPs.

(ii) For a given Ag@SiO₂/Pt nanostructure, the light absorption in Ag is constant no matter how many Pt NPs are sitting around.

Although there are electromagnetic couplings between Pt NPs and Ag NP, the light absorption in Ag is 2–3 orders of magnitude higher than that in Pt (see Ag(25 nm)@SiO₂(4 nm)/Pt as an example in Figure S8, and other structures in Figure S9 and S12) due to the difference in volume of the structures. Thus, the light absorption in Ag is deemed to be a constant.

(iii) The amount of light scattering from Ag that is absorbed by adjacent Pt NPs is small, thus the scattering from the whole structure is considered constant.

The light scattering from Ag is partially absorbed by adjacent Pt NPs. It is a very small part comparing with the original scattering cross section (see Ag(25 nm)@SiO₂(4 nm)/Pt in Figure S8 as an example, and other structures in Figure S9 and S12), so the scattering from Ag can still be considered as a constant, which equals the scattering from the whole structure.

Based on above assumptions, it is assumed that if more than one Pt NP is deposited around each Ag@SiO₂ structure, the total absorption in all Pt NPs is proportional to the position-averaged light absorption in one Pt NP, and linearly scales with increasing the number of Pt NPs. Thus, our FDTD

analysis focused on structures that contain only one Pt NP, but we justified that the results are scalable to the analysis of the realistic Ag@SiO₂/Pt structures in our experimental system, through multiplication of the optical response of one Pt NP by the average number of Pt NPs expected per Ag@SiO₂/Pt antenna-reactor complexes in the experimental system.

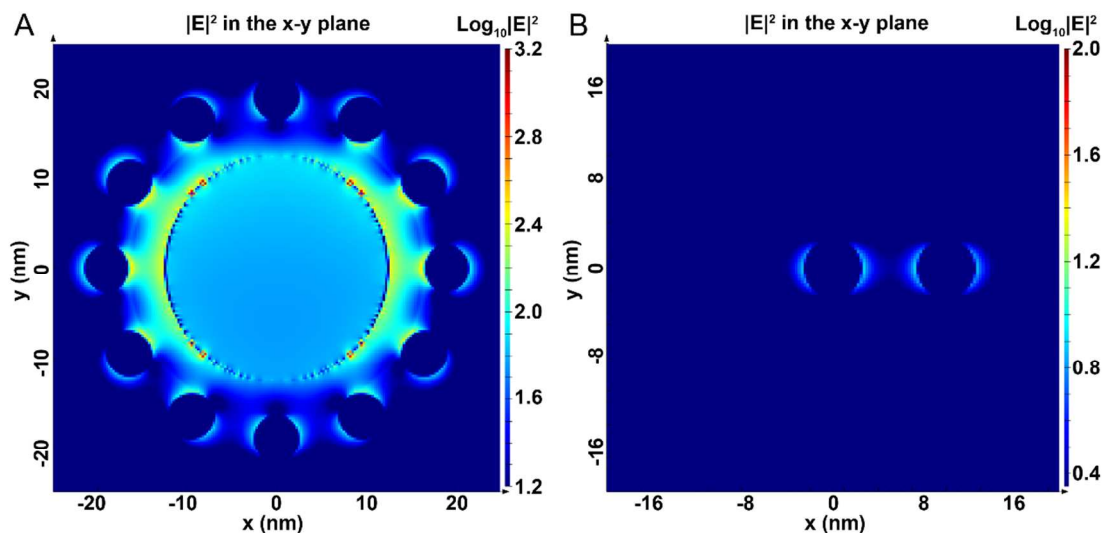


Figure S7. Electromagnetic distribution at the x - y plane for (A) structure with 12 Pt NPs located around Ag(25 nm)@SiO₂(4 nm) and (B) two Pt NPs with a 5 nm distance.

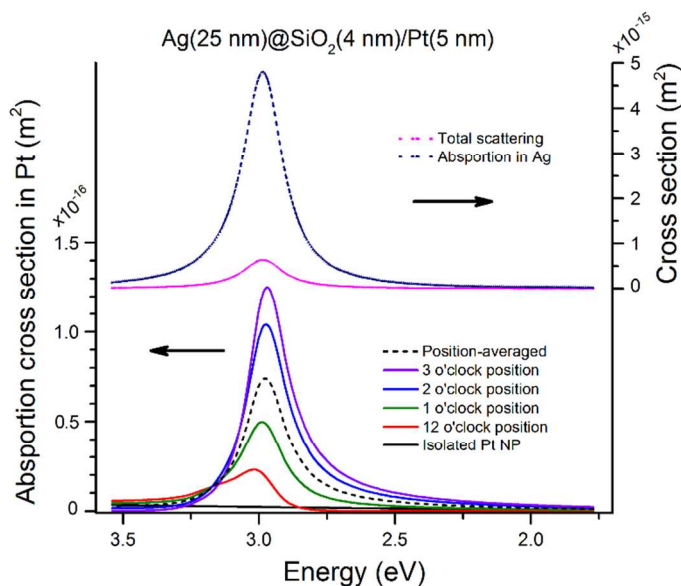


Figure S8. Absorption cross section in Pt (left axis) at four different positions and absorption and scattering cross section in Ag (right axis) for Ag(25 nm)@SiO₂(4 nm)/Pt.

4.2 Calculation process for defined metrics

We monitored the light scattering from the whole structure (Ag@SiO₂/Pt), and light absorption in Pt and Ag separately, under the illumination of polarized light with a wavelength range of 700–350 nm. In order to elucidate the absorption property of Pt under broadband light illumination, an area integral of each spectrum was used, instead of the maximum light absorption at a specific wavelength. For the area integral of each spectrum, energy (eV) rather than wavelength (nm) was used as the x -axis. Actually, using energy makes more sense when integrating the spectrum, where the area means the total energy dissipated in Pt NP.

Wavelength-integrated total Pt absorption cross section for Pt at position # n ($Abs_{Pt}^{\#n}$) was calculated by integrating the wavelength-dependent absorption curve:

$$Abs_{Pt}^{\#n} = \int_{1.77 \text{ eV}}^{3.54 \text{ eV}} Abs_{Pt}^{\#n}(E) \cdot dE \quad (\text{Eq. S1})$$

where E indicates the energy of a photon, which ranges from 1.77 to 3.54 eV (i.e., light wavelength range 700–350 nm). $Abs_{Pt}^{\#n}$ was defined as the absorption in Pt for Ag@SiO₂/Pt with one Pt NP at # n position, where # n = 1, 2, 3, or 4 represents 0°, 30°, 60°, or 90° position at the x - y plane, respectively.

Position-averaged, wavelength-integrated Pt absorption cross section (Abs_{Pt}) was calculated as

$$Abs_{Pt} = \sum_{n=1}^4 \frac{1}{4} \int_{1.77 \text{ eV}}^{3.54 \text{ eV}} Abs_{Pt}^{\#n}(E) \cdot dE \quad (\text{Eq. S2})$$

Thus, position-averaged, wavelength-integrated **Pt absorption enhancement** (ENH_{Abs}) was calculated as

$$ENH_{Abs} = \sum_{n=1}^4 \frac{1}{4} \int_{1.77 \text{ eV}}^{3.54 \text{ eV}} \frac{Abs_{Pt}^{\#n}(E)}{Abs_{Pt}^*(E)} dE \quad (\text{Eq. S3})$$

where Abs_{Pt}^* is the absorption in an isolated Pt NP without the Ag@SiO₂ structure. This defines the total enhancement in broad band Pt absorption induced by the Ag LSPR. It should be point out that the position-averaged ENH_{Abs} can also be defined prior to wavelength integration to interrogate the wavelength (photon energy) dependence.

For Ag@SiO₂/Pt heterostructures with 1.0 wt % Pt loading, the number of Pt NPs located on ONE Ag@SiO₂ heterostructure (N_{Pt}) relies on the size of Ag core. In ONE Ag@SiO₂ heterostructure, the mass of each component (Ag core, Pt NP, and SiO₂ shell) were respectively calculated as

$$m_{Ag} = \frac{4}{3}\pi r_{Ag}^3 \cdot \rho_{Ag} \quad (\text{Eq. S4})$$

$$m_{Pt} = \frac{4}{3}\pi r_{Pt}^3 \cdot \rho_{Pt} \quad (\text{Eq. S5})$$

$$m_{SiO_2} = \frac{4}{3}\pi [(r_{Ag} + 10 \text{ nm})^3 - r_{Ag}^3] \cdot \rho_{SiO_2} \quad (\text{Eq. S6})$$

where ρ_{Ag} , ρ_{Pt} and ρ_{SiO_2} are the density of Ag, Pt, and SiO₂, respectively. So, by solving the equation

$$1.0 \% = \frac{N_{Pt} \cdot m_{Pt}}{N_{Pt} \cdot m_{Pt} + m_{Ag} + m_{SiO_2}} \quad (\text{Eq. S7})$$

we obtained N_{Pt} for all of our proposed structures, and the results are summarized in Table S2.

Then, after calculated the wavelength-integrated total Ag absorption cross section (Abs_{Ag}), which expresses as

$$Abs_{Ag} = \int_{1.77 \text{ eV}}^{3.54 \text{ eV}} Abs_{Ag}(E) \cdot dE \quad (\text{Eq. S8})$$

we further defined the position-averaged, wavelength-integrated **absorption quality factor** (Q_{Abs}) as

$$Q_{Abs} = \frac{N_{Pt} \cdot Abs_{Pt}}{Abs_{Ag}} \quad (\text{Eq. S9})$$

Because Ag could potentially absorb a significant portion of the incoming light flux, Q_{Abs} is critical for understanding the competition between Pt and Ag in the absorption of incoming photons. Similarly, the position-averaged Q_{Abs} can also be defined prior to wavelength integration to interrogate the wavelength (photon energy) dependence.

At last, we defined the position-averaged, wavelength-integrated **light utilization coefficient** (U_{Light}) as

$$U_{\text{Light}} = \frac{N_{\text{Pt}} \cdot \text{Abs}_{\text{Pt}}}{N_{\text{Pt}} \cdot \text{Abs}_{\text{Pt}} + \text{Abs}_{\text{Ag}} + \text{Scat}} \quad (\text{Eq. S10})$$

where *Scat* is the wavelength-integrated scattering cross section of the whole heterostructure.

Ag LSPR can decay through radiative and non-radiative channels, which may have a negative influence on the overall photocatalytic performance of the system, as Ag cannot drive catalysis in the proposed core-shell geometry. So U_{Light} , which defines the fraction of photons that are absorbed in Pt and are used to drive photocatalysis, is critical for understanding the utilization effectiveness of light and the photocatalytic performance of structures proposed here, when operating photocatalysis under conditions where all impinging photons will be absorbed. Similarly, the position-averaged U_{Light} can also be defined prior to wavelength integration to interrogate the wavelength (photon energy) dependence.

Table S2. Number of Pt NPs (N_{Pt}) located on ONE Ag@SiO₂ structure with varying Ag NP size.

Structure on which a Pt NP is deposited	N_{Pt}
Ag(12 nm)@SiO ₂ (10 nm)	0.32
Ag(25 nm)@SiO ₂ (10 nm)	1.22
Ag(50 nm)@SiO ₂ (10 nm)	6.66
Ag(100 nm)@SiO ₂ (10 nm)	45.0
SiO ₂ (50 nm)	1.01

4.3 Dependence of optical properties on thickness of SiO₂ shell

To analyze the dependence of ENH_{Abs} and Q_{Abs} on the thickness of SiO₂ shell for Ag LSPR enhanced light absorption in Pt, we performed FDTD simulations for Ag@SiO₂/Pt structures that contain one Pt NP placed on the surface of Ag@SiO₂ with 25 nm Ag core and varying thicknesses (4, 10, and 20 nm) SiO₂ shell. The cross sections when placing Pt NP at four different positions were calculated (Figure S9). Figure S10A shows the position-averaged light absorption cross sections in Pt and Ag. It is clearly observed that absorption in Pt is strongly influenced by the Ag LSPR, due to the very similar shapes of the absorption spectra. For an isolated Pt NP alone, by contrast, a gradual decrease in absorption is seen as the photon energy decreases. Ag and Pt absorption peaks redshift with increasing SiO₂ thickness. Furthermore, the Pt absorption cross section significantly decreases as the SiO₂ thickness increases, due to the weakened coupling with the Ag near fields. For the Ag(25 nm)/Pt structure without an SiO₂ shell, Pt exhibits a significantly larger absorption cross section relative to structures with the SiO₂ shell, which is attributed to the strongest near-field enhancement at the surface of Ag.

The wavelength-dependent Pt ENH_{Abs} spectra for Ag(25 nm)@SiO₂ with different SiO₂ shell thicknesses are plotted in Figure S10B, which are essentially identical in spectral shape to the Pt absorption cross sections (Figure S10A). However, we find that the wavelength-dependent Q_{Abs} and U_{Light} are quite low for all structures that include an SiO₂ shell, and exhibits a characteristic negative peak at 2.8–3.0 eV (Figure S10C and S10D). This may result from several aspects. First, for a 25 nm Ag NP, absorption cross section is much larger than scattering cross section (Figure S9), thus a relatively large fraction energy stored in LSPR excitation would be dissipated in Ag rather than in Pt. Second, in these structures, the Pt absorption peak is slightly red-shifted from the Ag absorption peak (Figure S10A). Hence, Q_{Abs} or U_{Light} at the energy of ~3.0 eV is extremely low because of the absolute predominance of Ag absorption. Importantly, at all photon energies, Q_{Abs} or U_{Light} increases with decreasing SiO₂ thickness. Above comparison demonstrates that a thinner SiO₂ shell is highly advantageous facilitating all of the three metrics, due to the efficient coupling between the near fields of the 25 nm Ag NP and Pt NP, which is confirmed by electromagnetic field distribution study.

Figure S11 shows the electromagnetic field distributions for each structure at wavelengths of Pt

ENH_{Abs} maxima. As the SiO_2 shell thickness increases, the maxima of electromagnetic field energy density at Pt surface of each structure are respectively 4300-, 660-, 125-, and 30-fold enhanced when comparing with that of isolated Pt NP alone, which has a consistent trend with the Pt absorption enhancements.

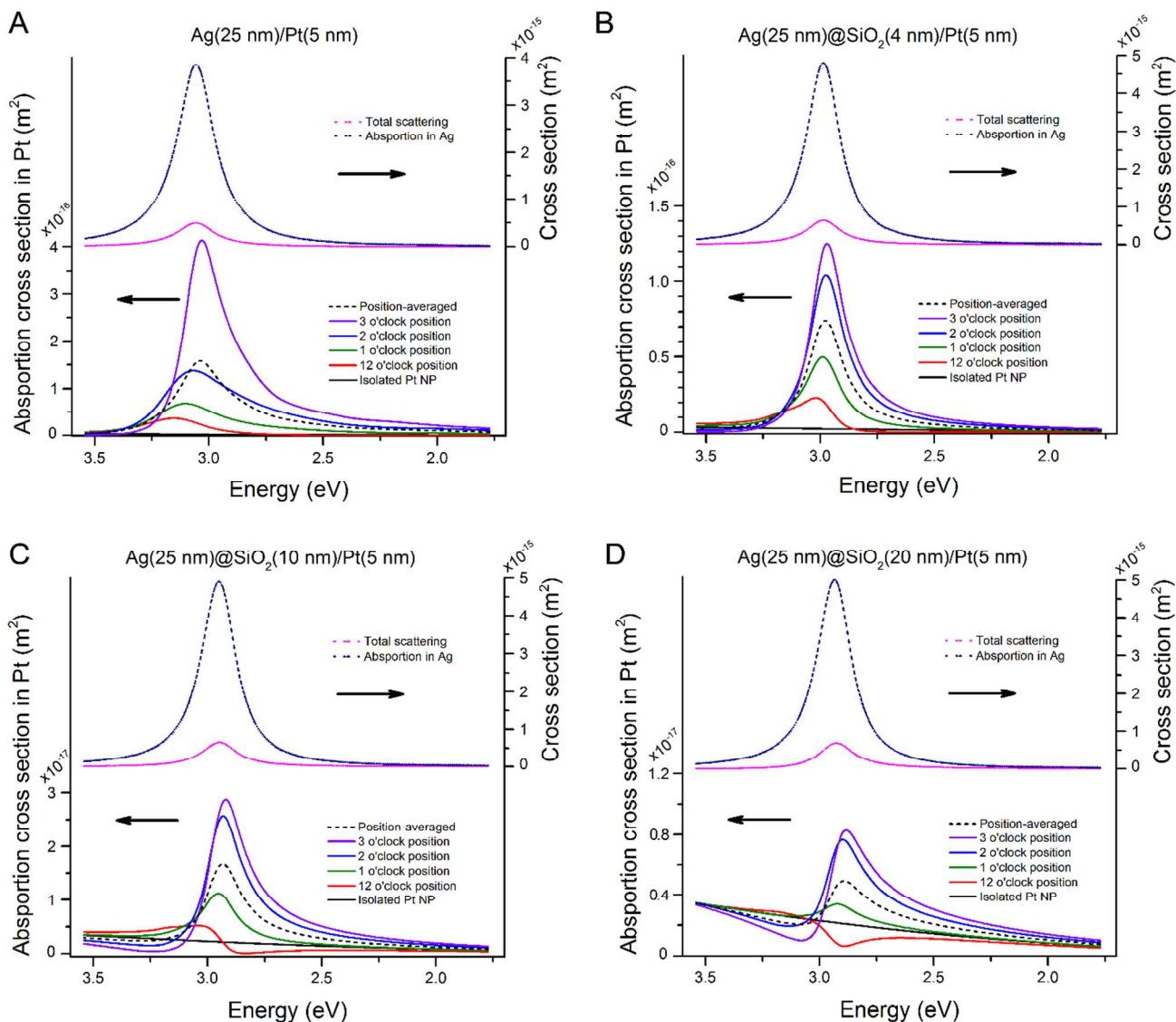


Figure S9. Absorption cross section in Pt (left axis) at four different positions and absorption and scattering cross section in Ag (right axis) for each $Ag@SiO_2/Pt$ heterostructure that contains 25 nm Ag core and SiO_2 shell with varying thicknesses, i.e., (A) 0 nm, (B) 4 nm, (C) 10 nm, and (D) 20 nm.

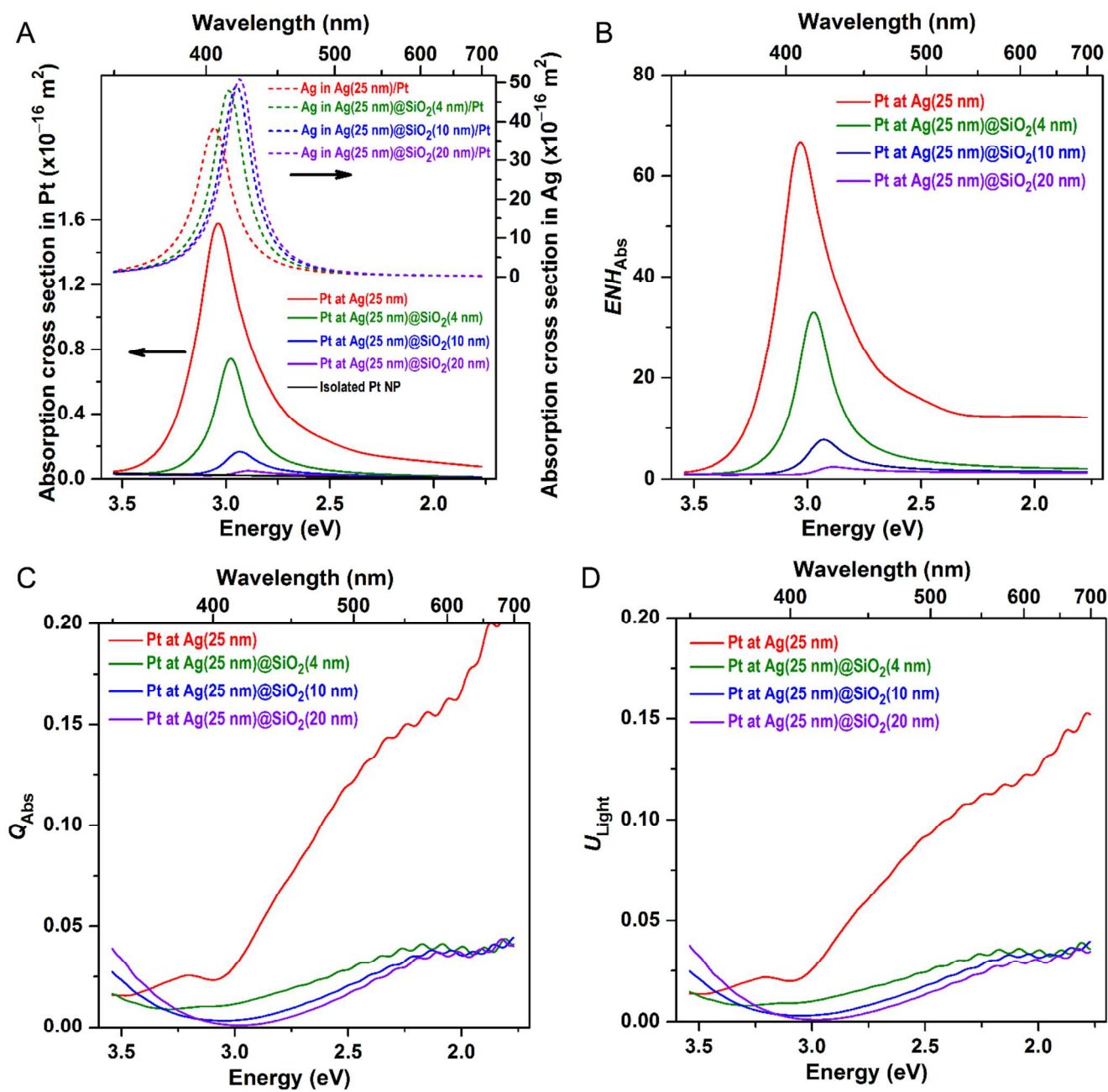


Figure S10. Absorption cross section in Pt (left axis) and Ag (right axis) (A), ENH_{Abs} (B), Q_{Abs} (C), and U_{Light} (D) as a function of wavelength for Ag@SiO₂/Pt heterostructures comprised of 25 nm Ag core and SiO₂ shell with various thicknesses.

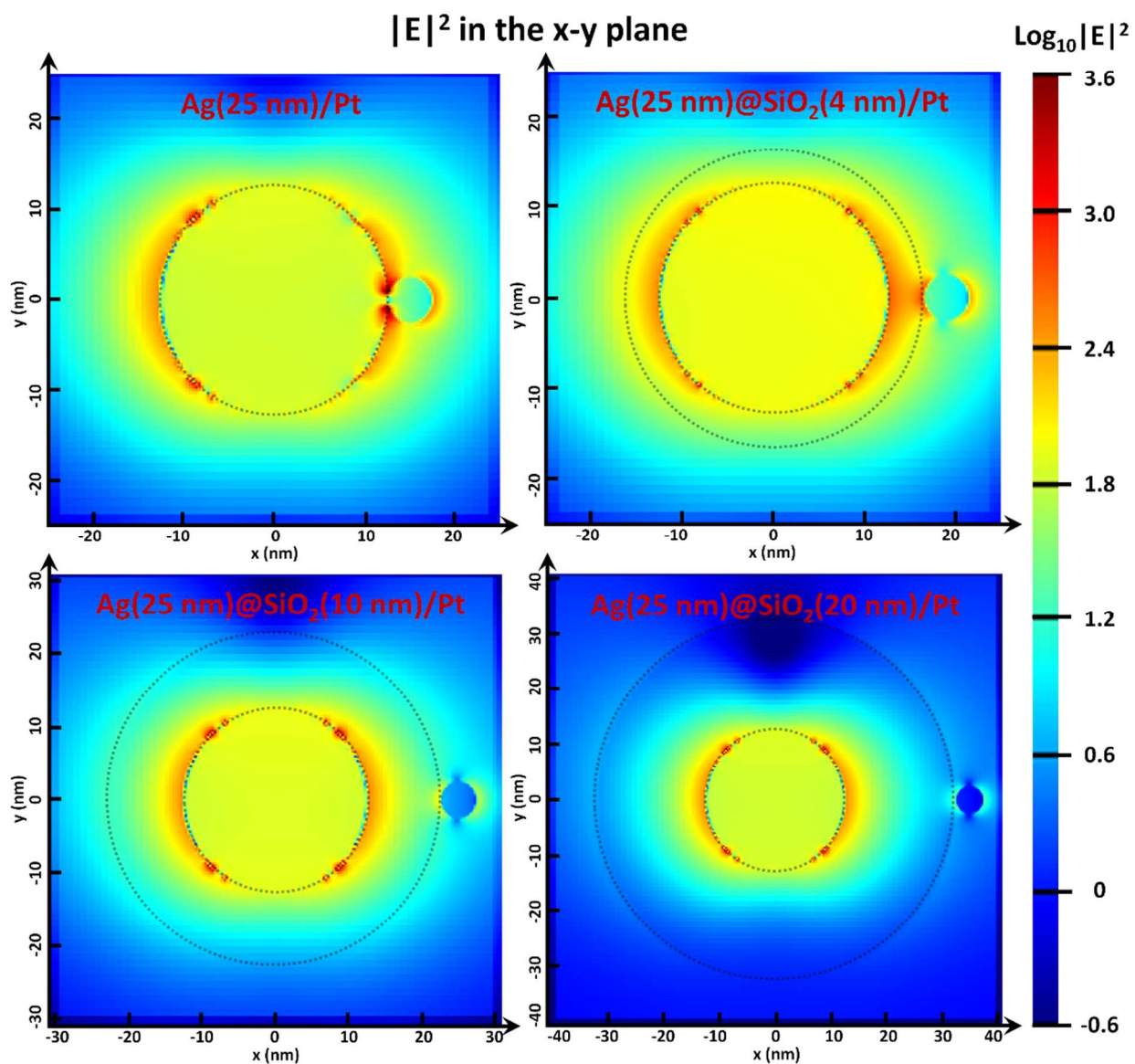


Figure S11. Electromagnetic field distributions in the x - y plane at the wavelengths corresponding to Pt absorption maxima (409 nm for Ag(25 nm)/Pt, 417 nm for Ag(25 nm)@SiO₂(4 nm)/Pt, 425 nm for Ag(25 nm)@SiO₂(10 nm)/Pt, and 430 nm for Ag(25 nm)@SiO₂(20 nm)/Pt).

4.4 Dependence of optical properties on size of Ag core

Ag NP size may be critical in further optimizing these systems, as it is known that LSPR decay channels are changed with increased particle size.^[9] Therefore, Ag NPs with varying sizes (12, 25, 50, and 100 nm) were employed, with a constant 10 nm SiO₂ shell. The cross sections when placing Pt NP at four different positions were calculated for each structure (Figure S12 and S13).

The 50 nm Ag NP core provides the maximum ENH_{Abs} in Pt (Figure 3C). We defined performance metrics to evaluate plasmon-enhanced Pt NPs absorption in the examined heterostructures (Section 4.2, Supporting Information). They are: the absorption quality factor (Q_{Abs}), which is the ratio between the photon absorption cross sections of Pt and Ag in the heterostructures (Eq. S9); and the light utilization coefficient (U_{Light}), which defines the fraction of photons absorbed in Pt compared to other fates, such as scattering from the heterostructure and absorption by the Ag NP (Eq. S10). Q_{Abs} and U_{Light} generally address the competitive performance of photon absorption in the heterostructures and the utilization effectiveness of light, respectively.

The wavelength-dependent Q_{abs} and U_{Light} for Pt NPs with different Ag NP core diameters are plotted in Figure S14. When considering how effective the heterostructure is at directing the photon absorption to Pt, where photocatalysis can occur (Q_{abs}), the 100 nm Ag NPs provide the best performance due to their low inherent absorption cross sections. When considering the fraction of light absorbed by the Pt NP, compared to all other possible fates (U_{Light}), however, quite complex behavior is observed, where near the dipolar plasmon resonance wavelength the largest Ag NPs perform best, while at longer photon wavelengths smaller Ag NP perform best. By comparing the relative trends in these three performance metrics with the trends in photocatalysis shown in Figure 2, it is clear that none of the metrics can fully capture the observed Ag size-dependent photocatalytic behavior.

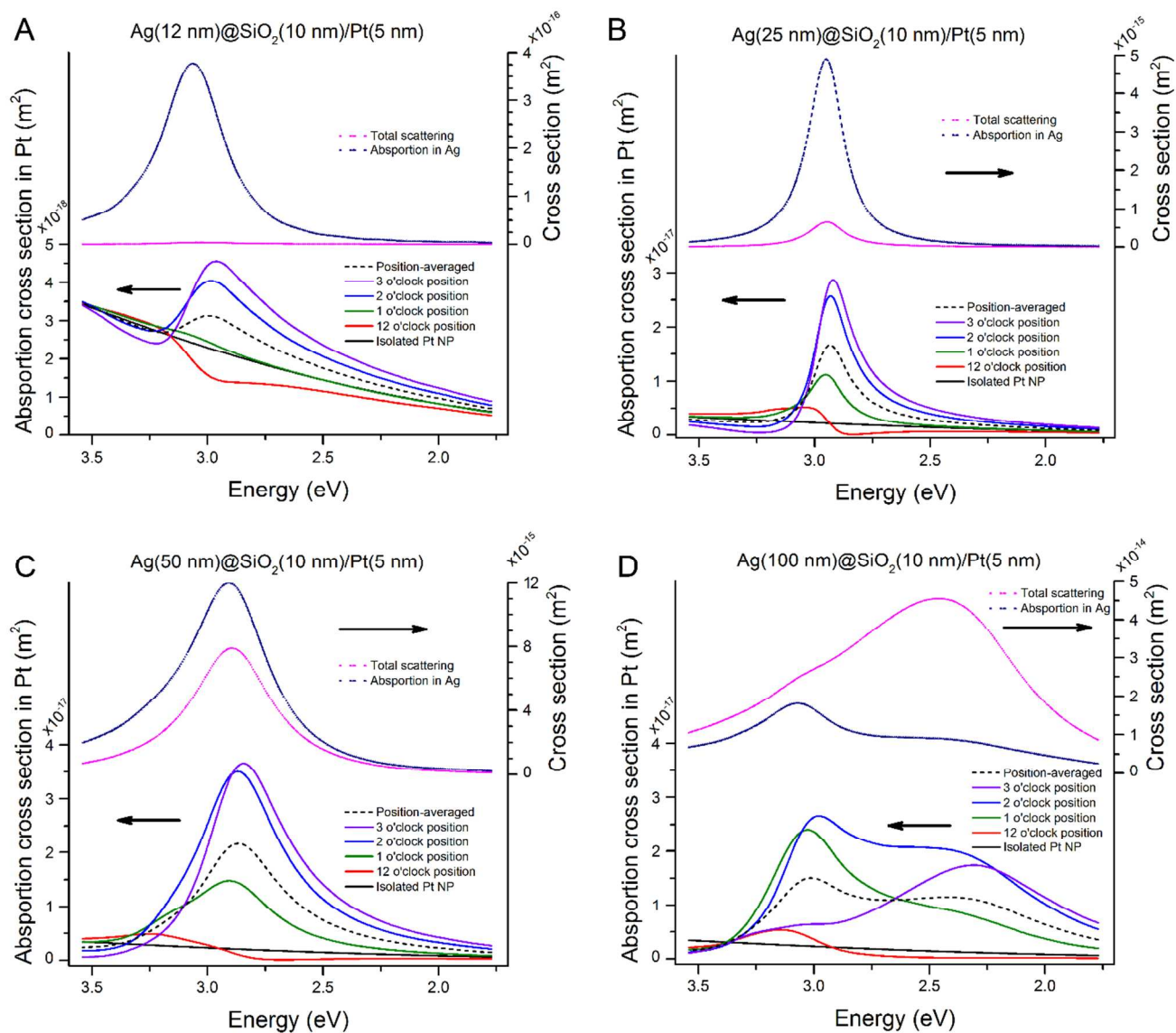


Figure S12. Absorption cross section in Pt (left axis) at four different positions and absorption and scattering cross section in Ag (right axis) for each Ag@SiO₂/Pt heterostructure that contains 10 nm SiO₂ shell and Ag core with varying diameters, i.e., (A) 12 nm, (B) 25 nm, (C) 50 nm, and (D) 100 nm.

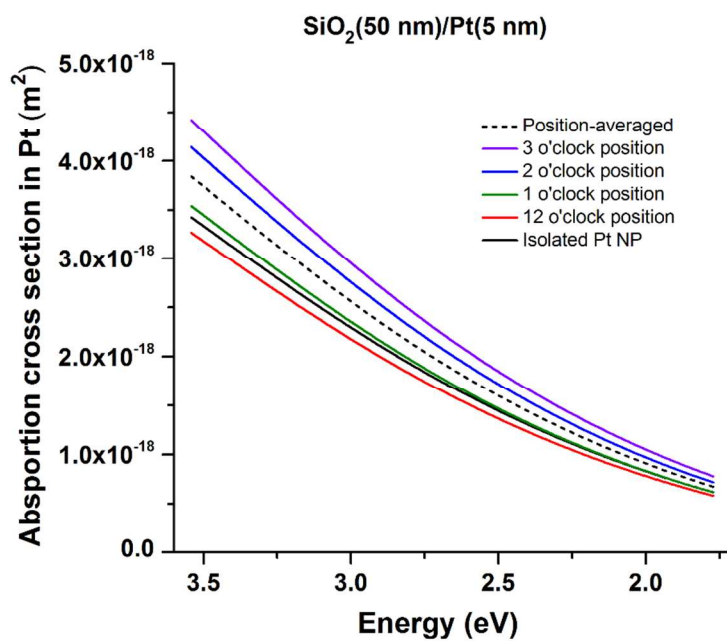


Figure S13. Absorption cross section in Pt at four different positions (red, green, blue, and purple curves) and Pt position-averaged absorption cross section (dotted black curve) for $\text{SiO}_2(50 \text{ nm})/\text{Pt}$ structure. Absorption cross section in an isolated Pt NP is also shown (solid black curve).

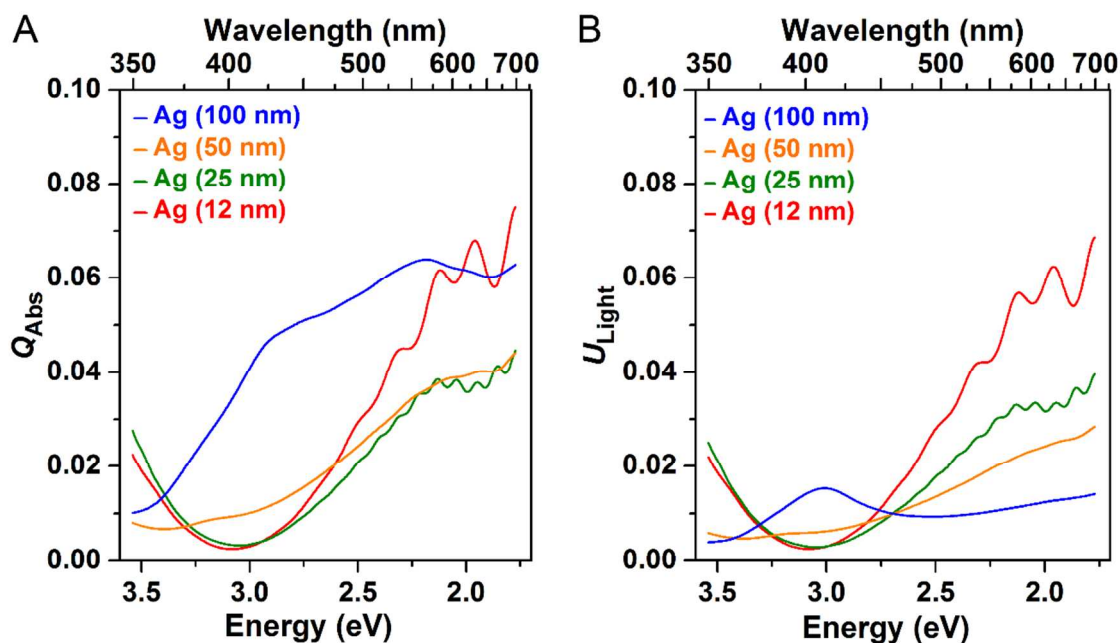


Figure S14. (A) Absorption quality factor (Q_{Abs}), and (B) light utilization coefficient (U_{Light}) for $\text{Ag}@/\text{SiO}_2/\text{Pt}$ heterostructures with different Ag NP sizes and a constant 10 nm SiO_2 shell.

4.5 Photocatalysis on 2-D films of Ag@SiO₂/Pt particles

In the study of broadband photocatalysis, if photocatalysis is carried out on 2-D films of Ag@SiO₂/Pt complexes (Figure S15A), where all Pt NPs are illuminated with equal photon flux and the absorption efficiency by the film is much less than 100% (i.e., photocatalysis doesn't run in the light-limited regime), ENH_{Abs} is the only critical metric that needs to be considered. Thus, Q_{Abs} and U_{Light} are less important because there are excess photons.

It is also critical to consider whether the photocatalytic application requires broadband absorption enhancement in the non-plasmonic nanostructure, or whether a transfer of resonant photons of a specific energy is preferred. In the case of enhancing the catalytic selectivity via plasmonically enhanced Pt absorption at specific wavelength, it would be most beneficial to have an Ag core that provides the largest percentage of Pt absorption enhancement at the desired wavelength, rather than a broadband absorption enhancement. For example, we recently showed that photon absorption in Pt clusters at the wavelength regime around 450 nm uniquely enhanced selectivity in the preferential CO oxidation reaction.^[4] Figure S15B and S15C shows the percentage of total Pt absorption enhancement that occurs in the wavelength range of 450±10 nm for Ag@SiO₂/Pt complexes with 10 nm SiO₂ shell and varying diameters Ag core. It is apparent in the figure that 50 nm Ag core will, to the maximum extent, achieve the LSPR enhanced selectivity for the previously demonstrated preferential CO oxidation reaction.

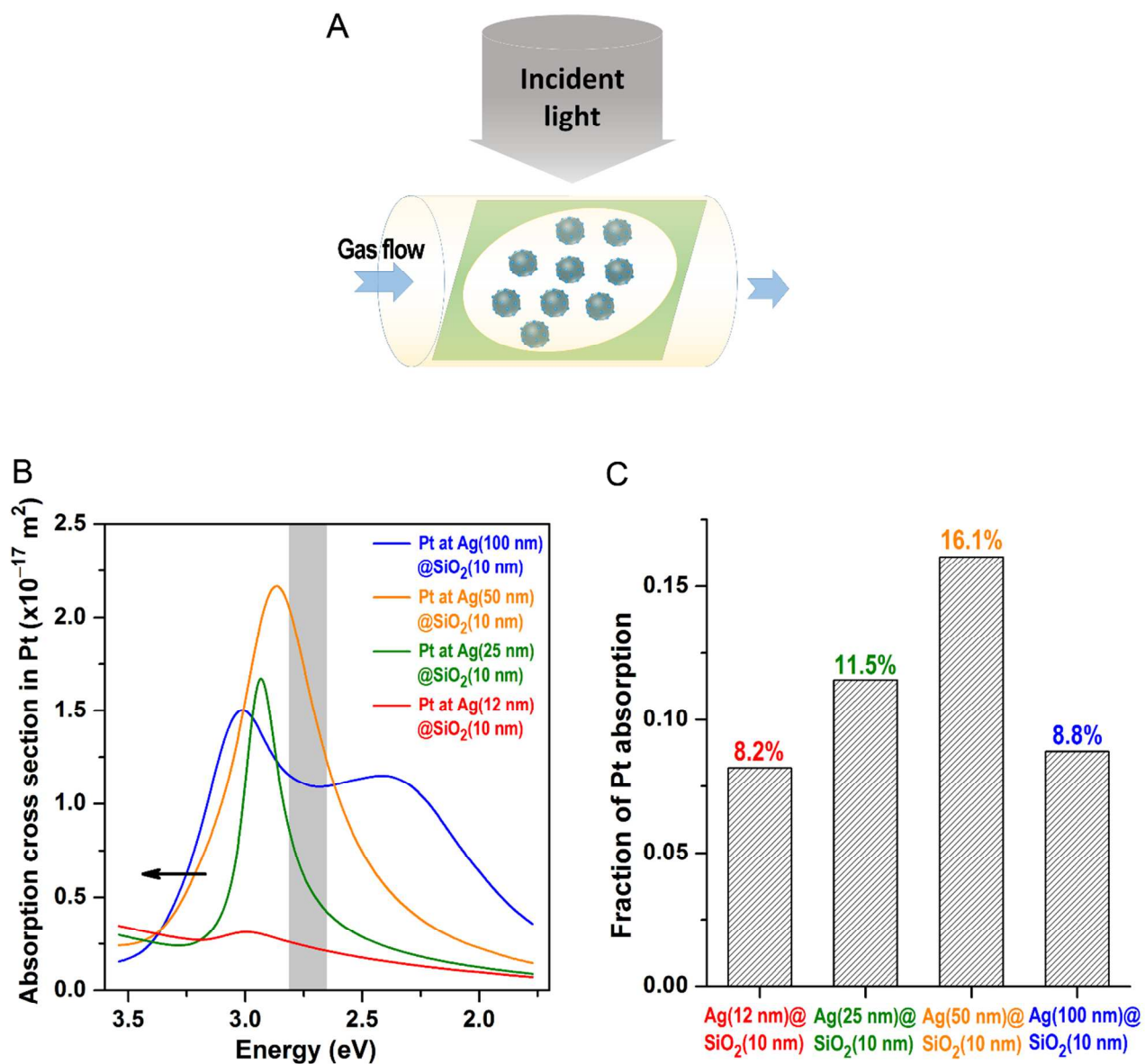


Figure S15. (A) Schematic of broadband photocatalysis on 2-D films of Ag@SiO₂/Pt heterostructures. (B, C) Description of the design rules for wavelength selectivity in photocatalysis. (B) Pt absorption cross section for Ag@SiO₂/Pt heterostructures with 10 nm SiO₂ shell and varying diameters Ag core. The shaded region shows the limits of integration (2.70–2.82 eV. i.e., wavelength range 460–440 nm) when comparing the wavelength selectivity of each structure. (C) The percentage of broadband Pt ENH_{Abs} occurring in the wavelength-selective range of 450 ± 10 nm.

5. Supplementary discussions on Monte Carlo simulations

Table S3. Density of Ag@SiO₂/Pt antenna-reactor complexes in Monte Carlo simulations

Structure	Density of complexes (particles/cm ⁻³)
Ag(12 nm)@SiO ₂ /Pt	$1.39 \times 10^{+15}$
Ag(25 nm)@SiO ₂ /Pt	$3.64 \times 10^{+14}$
Ag(50 nm)@SiO ₂ /Pt	$6.69 \times 10^{+13}$
Ag(100 nm)@SiO ₂ /Pt	$9.89 \times 10^{+12}$

Due to the scattering and absorption of Ag@SiO₂/Pt structures, the amount of antenna-reactor complexes that will be illuminated in the reactor are different (Figure S16A). So the data showing the decay length of absorption events along the propagation direction of the light (*z*-axis) is important (Figure S16B). It is noted that an exponential fit was made to the absorption events in the *z*-direction, and the penetration depth is the value where the light intensity decays to 1/*e* of the maximum (incident light).

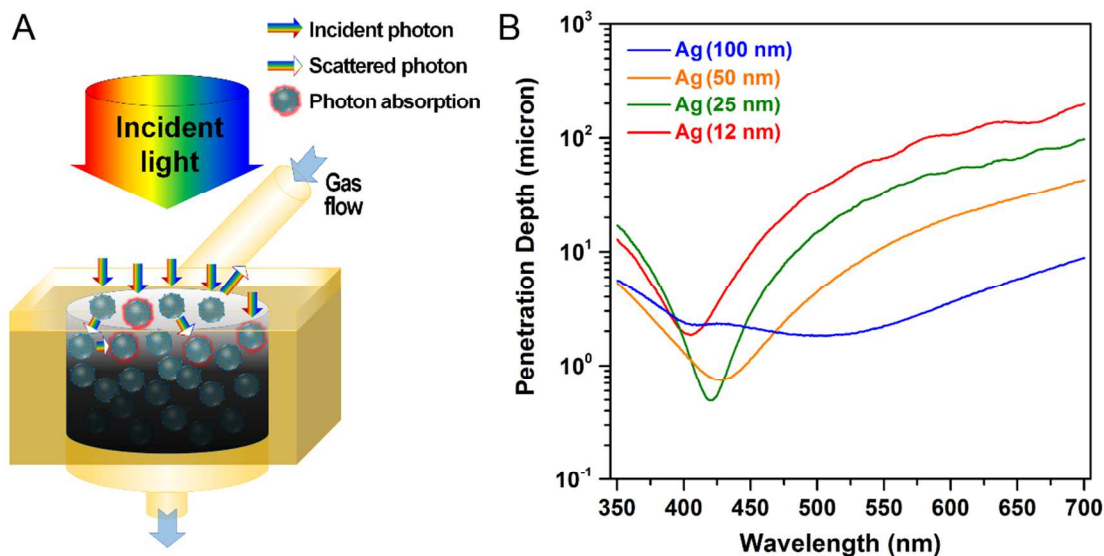


Figure S16. (A) Cartoon of broadband photocatalysis of Ag@SiO₂/Pt heterostructures in 3D reactor geometry. (B) Wavelength-dependent penetration depth for the four proposed heterostructures. The depth is the value where the light intensity decays to 1/*e* of the maximum (incident light).

6. Supplementary discussions on electromagnetic field enhancements

The enhanced electromagnetic field distributions on each structure at the wavelengths of Pt absorption maxima is shown in Figure S17. With increasing Ag size, the maxima of electromagnetic field energy density at Pt surface of each structure are respectively 17-, 125-, 150-, and 110-fold enhanced when comparing with that of isolated Pt NP alone. The field enhancement values shown here are the values at the locations on Pt NP surface with strongest enhancements. As the Ag size increases, the strong scattering LSPR decay channel for Ag NP can penetrate through thicker SiO₂ shells and spread to a broader area, enabling the field distribution on Pt NP surface more uniform. Thus, the enhanced field is increasingly pulled from the Ag NP surface and localized on Pt, which contributes to the continuous increase of Q_{Abs} and U_{Light} at resonance wavelength regime for Ag@SiO₂/Pt with larger Ag NPs (Figure S14A and S14B). On the other hand, the electromagnetic field localization on Pt depends more strongly on the position where the Pt NP is deposited around the Ag@SiO₂ particle when the Ag NP size is greater than 70 nm, where the quadrupole resonance becomes dominant.^[9] The field distribution plots for Ag@SiO₂/Pt with Pt NP placed at 60° position (Figure S17D) show better coupling of Pt to quadrupole component of LSPR from larger Ag NPs.

In Figure 4C, the electromagnetic field enhancements were calculated as weighted averages with respect to the broadband spectrum of the light source in photocatalytic measurements followed by normalization, to allow comparison to the photocatalytic measurements under the broadband photon flux. Typically, at a given wavelength, the highest electromagnetic field enhancement value at Pt surface was picked for each of the 4 Pt positions. So, an average of these 4 values was defined as the electromagnetic field enhancement for this wavelength. A series of wavelength points, which are consistent with that used in wavelength-dependent QY measurements, i.e., 350, 400, 425, 450, 475, 500, 550, 600, 650, and 700 nm, are selected for this calculation. These results are shown in Figure S18. Then, an integration for these averages at different wavelengths was conducted by calculating the weighted average with respect to the spectrum of the broadband white light (Figure S3).

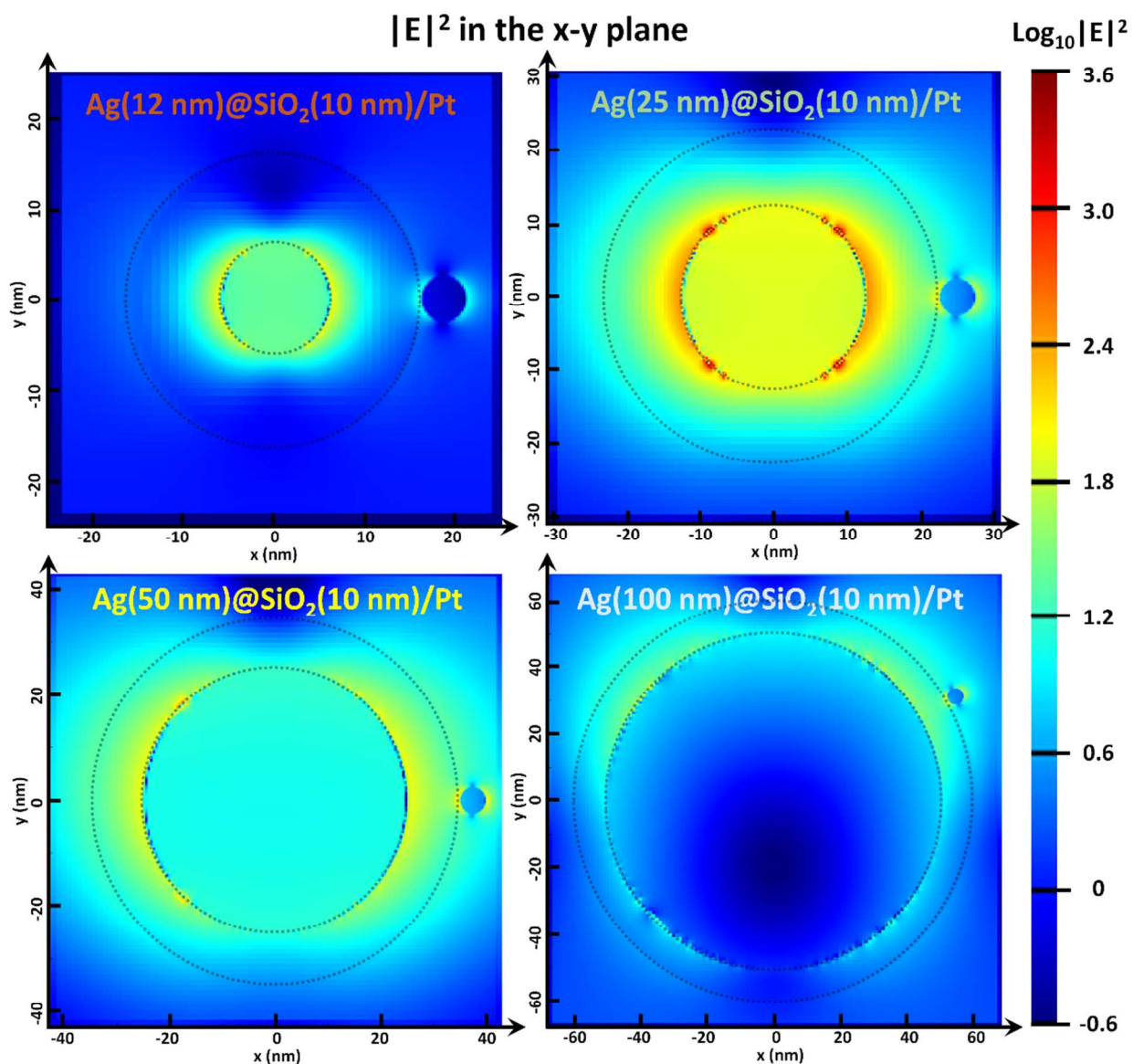


Figure S17. Electromagnetic field distributions in the x - y plane at the wavelengths corresponding to Pt absorption maxima (418 nm for Ag(12 nm)@SiO₂(10 nm)/Pt, 425 nm for Ag(25 nm)@SiO₂(10 nm)/Pt, 436 nm for Ag(50 nm)@SiO₂(10 nm)/Pt, and 416 nm for Ag(100 nm)@SiO₂(10 nm)/Pt).

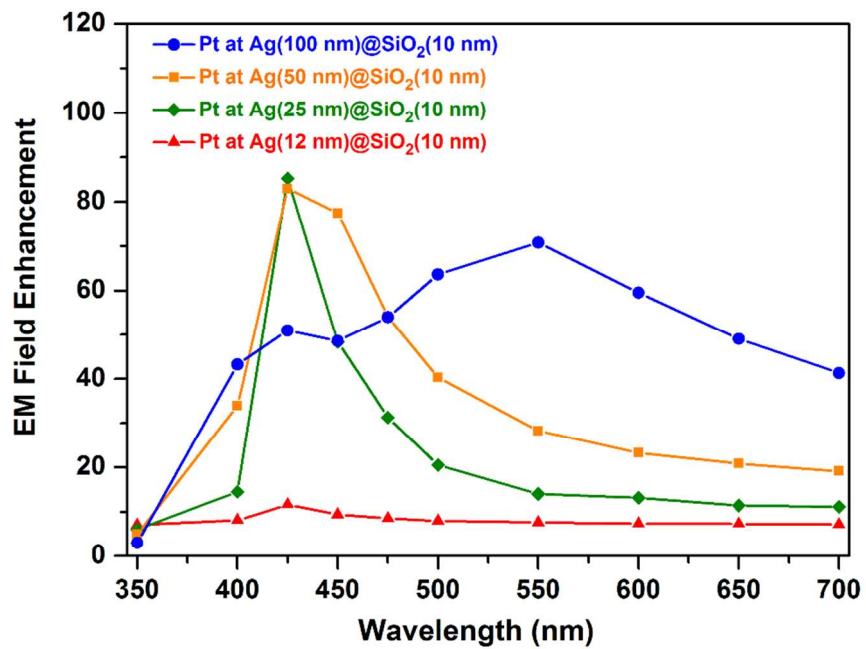


Figure S18. Wavelength-dependent electromagnetic field enhancement values at the Pt surface for the four Ag@SiO₂/Pt heterostructures with different Ag NP sizes.

Supplementary References

- (1) Bastús, N. G.; Merkoçi, F.; Piella, J.; Puntès, V. *Chem. Mater.* **2014**, *26*, 2836-2846.
- (2) Stöber, W.; Fink, A.; Bohn, E. *J. Colloid Interface Sci.* **1968**, *26*, 62-69.
- (3) Christopher, P.; Xin, H.; Linic, S. *Nat. Chem.* **2011**, *3*, 467-472.
- (4) Kale, M. J.; Avanesian, T.; Xin, H.; Yan, J.; Christopher, P. *Nano Lett.* **2014**, *14*, 5405-5412.
- (5) Christopher, P.; Xin, H.; Marimuthu, A.; Linic, S. *Nat. Mater.* **2012**, *11*, 1044-1050.
- (6) Haynes, W. M. *CRC Handbook of Chemistry and Physics, 95th Edition*; CRC press: Boca Raton, **2014**; Section 10, pp 240-243.
- (7) Hagemann, H. J., Gudat, W., and Kunz, C. *J. Opt. Soc. Am.* **1975**, *65*, 742-744.
- (8) Palik, E. D. *Handbook of Optical Constants of Solids. Vol. 3*; Academic press: San Diego, **1998**; pp 187-227.
- (9) Evanoff, D. D.; Chumanov, G. *J. Phys. Chem. B* **2004**, *108*, 13957-13962.